Supplemental Information: Perceptual load affects spatial tuning of neuronal populations in human early visual cortex

Benjamin de Haas, D. Samuel Schwarzkopf, Elaine J. Anderson and Geraint Rees

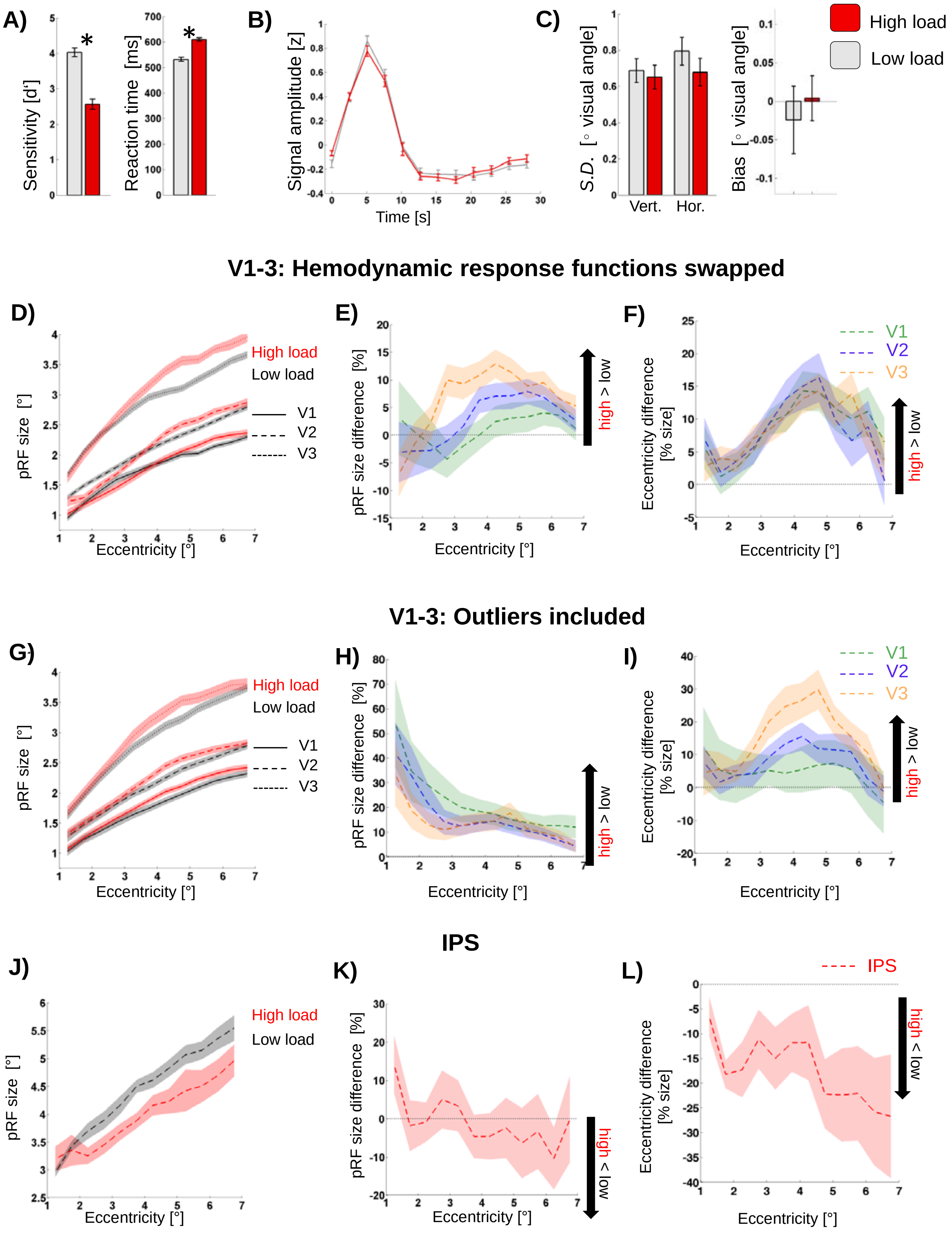
A)
Sensitivity [d']
Reaction time [ms]
*
*
B)
Signal amplitude [z]
Time [s]
C)
S.D. [° visual angle]
Vert.
Hor.
Bias [° visual angle]
High load
Low load
V1-3: Hemodynamic response functions swapped
D)
pRF size [°]
Eccentricity [°]
High load
Low load
V1
V2
V3
E)
pRF size difference [%]
Eccentricity [°]
high > low
F)
Eccentricity difference [% size]
Eccentricity [°]
V1
V2
V3
high > low
V1-3: Outliers included
G)
pRF size [°]
Eccentricity [°]
High load
Low load
V1
V2
V3
H)
pRF size difference [%]
Eccentricity [°]
high > low
I)
Eccentricity difference [% size]
Eccentricity [°]
V1
V2
V3
high > low
IPS
J)
pRF size [°]
Eccentricity [°]
High load
Low load
K)
pRF size difference [%]
Eccentricity [°]
high < low
L)
Eccentricity difference [% size]
Eccentricity [°]
IPS
high < low

Figure S1

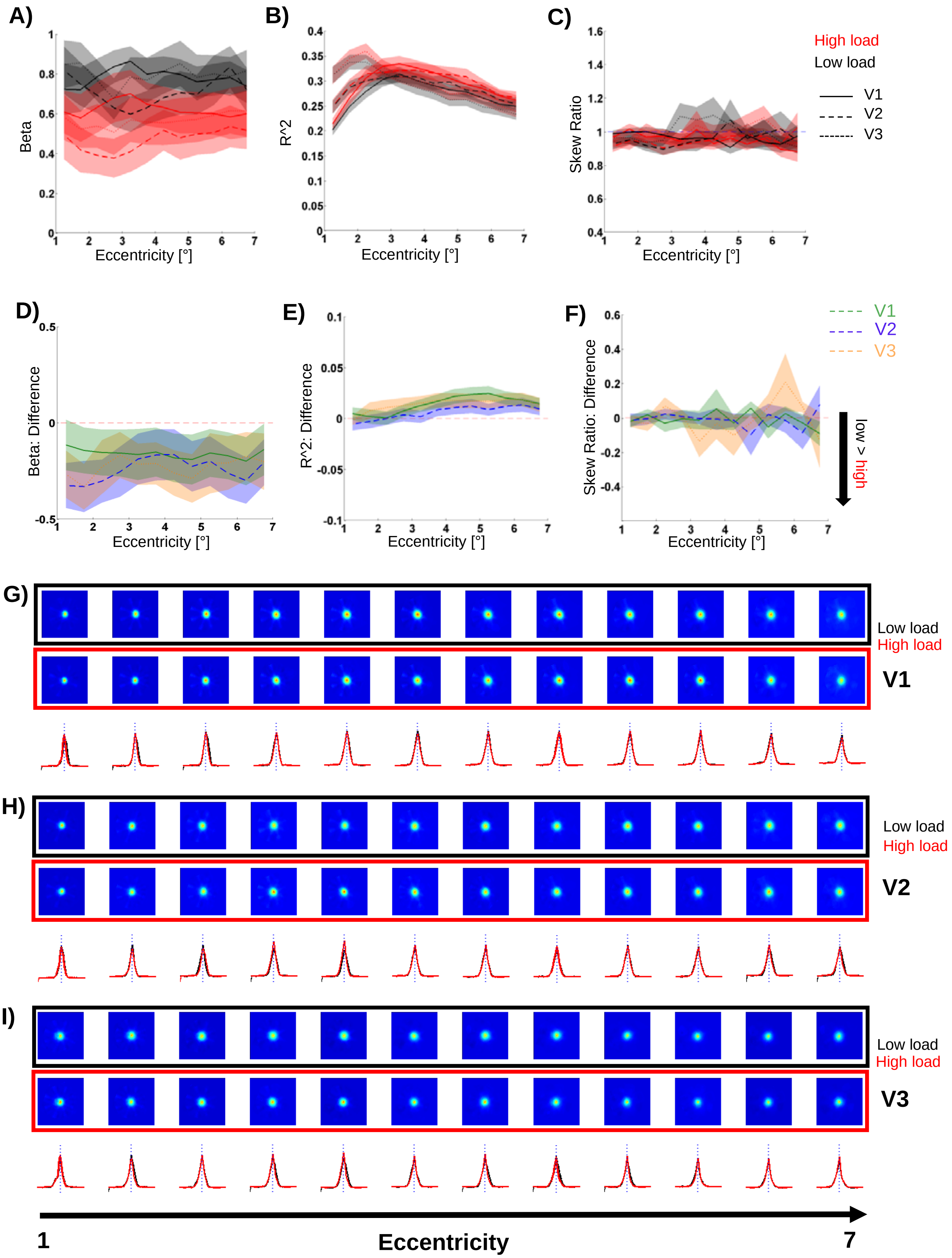
A)
Beta
Eccentricity [°]
B)
R^2
Eccentricity [°]
C)
Skew Ratio
Eccentricity [°]
High load
Low load
V1
V2
V3
D)
Beta: Difference
Eccentricity [°]
E)
R^2: Difference
Eccentricity [°]
F)
Skew Ratio: Difference
Eccentricity [°]
V1
V2
V3
low > high
G)
Low load
High load
V1
H)
Low load
High load
V2
I)
Low load
High load
V3
1
Eccentricity
7

Figure S2

Supplemental Figures

Figure S1. A-C: (A) Behavioural effects of load manipulation: Sensitivity and reaction times for target detection by condition. **(B)** Hemodynamic response to photic bursts for both conditions (averaged across participants). (**C**) Left hand side: Stability of eye position averaged across participants and stimulus sweeps. Right hand side: Bias of eye gaze towards the sweeping direction of mapping stimuli (averaged across participants and stimulus sweeps). **D-L**: Columns**:** (**D, G, J**) Absolute pRF size by condition; (**E, H, K**) Relative change of pRF size under high vs. low load; (**F,I, L**) Change of pRF eccentricity under high vs. low load (normalised by pRF size). Rows: (**D-F**) Reanalysis of data from V1-3 with hemodynamic response profiles swapped between conditions; (**G-I**) Reanalysis of data from V1-V3 including potential outliers; (**J-L**) Results for data from intraparietal sulcus (IPS). All bars and error bars (A-C) / lines and error shades (D-L) indicate mean +/- 1 standard error of the mean (SEM). For more details see Supplemental Experimental Procedures and Results.

Figure S2. (**A**) Amplitude parameters of hemodynamic response profiles for V1-3 by condition and eccentricity. (**B**) Coefficient of determination for pRF model fit by condition and eccentricity. Note that we fitted complete time series rather than across-run averages, rendering nominal goodness of fit values lower than those reported by other groups. (**C**) Skew ratio of reverse correlation pRF response profiles. A value of one indicates symmetry on the radial axis while values greater/smaller one indicate radial/central bias, respectively (see Supplemental Experimental Procedures and Results for more details). Color and line style in panels (**A-C**) indicate condition and visual area as detailed in the inset. Panels (**D-F**) show the difference values between conditions corresponding to values shown in panels (**A-C**); color indicates visual area as detailed in the inset. All lines and error shades indicate mean +/- 1 standard error of the mean (S.E.M.). **(G-I)** Response profiles for average pRFs by eccentricity and condition, as determined by reverse correlation analysis. Panels G,H and I show data from V1, 2 and 3, respectively. The top and middle rows of each panel show response profiles for the low and high perceptual load condition, respectively. Bottom rows of each panel show a cross-section of the response profiles (high load and low load profiles shown in red and black, respectively). Averages are specific to eccentricity bins ranging from 1 to 7 degrees visual angle in steps of half a degree and are sorted from left to right. Response profiles from different polar angle bins were rotated to a common reference frame such that the central-radial direction corresponds to the left-right axis in the image. For more details see Supplemental Experimental Procedures and Results.

Supplemental Experimental Procedures

Participants

Twenty-seven healthy participants with normal or corrected-to-normal visual acuity completed the experiment. Participants were recruited from the University College London (UCL) participant pool and gave written informed consent to take part in the study, which was approved by the UCL ethics committee. Data from one participant were excluded because reconstruction of the cortical surface failed, leaving 26 participants in the main analysis (mean age, 25 yrs, SD, 5 yrs; 14 females; 2 left handed). One participant took part in both versions of the experiment (conditions alternating between vs. within runs, see below), thus a total of 27 datasets were entered into the main analysis. Note that excluding the second dataset of the participant scanned twice did not change our results.

Stimuli

Central behavioural task - stimulus streams presented at central fixation were similar to those used in Schwartz *et al*. [S1] and consisted of a rapid serial visual presentation (RSVP) of coloured, upright or inverted crosses (height: 0.7° visual angle; colours: red, green, yellow, blue, black, white, light blue, purple, cyan, pink, orange, violet, brown) (see Figure 1 A). Each cross was presented on a grey background at the centre of the display for 500 ms with a gap of 250 ms between successive crosses. Targets in the low load condition were defined as red crosses (regardless of orientation); in the high load condition targets were defined as upright yellow and inverted green crosses. Stimuli did not differ between conditions and the proportion of targets among all stimuli was ~7.5% for either condition.

Task-irrelevant stimuli employed to map pRFs consisted of bars containing a dynamic, high contrast black (1.3 cd/m^2) and white (1997.5 cd/m^2) non-Cartesian grating. Note that local carrier luminance was time-varying with high frequency due to the dynamic nature of our stimulus and therefore unlikely to induce adaptation effects. None of our participants described any afterimages or other adaptation effects from these stimuli. Bars were ~1.5° visual angle wide and traversed a circular area with a radius of 9° visual angle centered on fixation. They moved in horizontal or vertical sweeps of 24 steps (step duration 2.55 s, corresponding to one TR) and spared a circular fixation aperture at the centre of the display, which was ~1.4° visual angle wide. The fixation aperture contained either the load stimuli or a fixation dot, which was ~0.2° visual angle wide. The background of the display was a uniform grey (547.5 cd/m^2). At all times, a subtly darker grey static ‘spider web’ was superimposed onto the entire display (mapping stimuli and background) to aid fixation compliance.

For each participant we acquired additional runs to estimate the individual, condition specific hemodynamic response function (HRF). We used sparse photic bursts for this, which filled the whole of the mapped area (stimulus duration: 2.55 s; inter-stimulus interval: 28.05 s). The stimulus contained the same pattern as the mapping bars.

Participants viewed stimuli via a mirror mounted at the head coil at a viewing distance of ~61 cm and at a resolution of 1024x768 pixels (24x18 degrees visual angle). All stimuli were programmed and presented in MATLAB (Mathworks, Ltd.) using the Psychophysics Toolbox 3 extension [S2, S3] (http://psychtoolbox.org).

Procedure

Each participant was familiarized with the load task outside the scanner and completed 4-8 mapping runs and two runs for HRF estimation. Load conditions alternated between runs for 14 participants (mapping runs of 148 volumes (~6 minutes), HRF runs of 104 volumes (~4.5 minutes) and within runs for 13 participants (mapping runs of 196 volumes (~8 minutes), HRF runs of 172 volumes (~7 minutes)).

Participants for which conditions alternated *between* runs (sample A) were notified of the upcoming condition by an instruction screen at the beginning of each run and the order of runs was counterbalanced between participants. Each mapping run was divided into 6 epochs of 24 TRs (or 61.2 s) and participants solved the ongoing load task throughout. The mapping stimulus traversed the display during 4 of the epochs, with each epoch corresponding to one cardinal sweep direction (order of directions pseudo-randomized but constant across load conditions). The third and sixth epochs were blank epochs containing no mapping stimuli. After four mapping runs, participants completed two HRF runs. During HRF runs, participants solved the ongoing load task while 10 photic bursts per run were presented in the surrounding visual field (see above, pRF mapping stimuli).

Participants for which conditions alternated *within* runs (sample B) were notified of the condition by a brief cue presented at the centre of the screen (both targets next to each other). Mapping runs were divided into 8 epochs of 24 TRs, with load conditions alternating after 4 epochs. Two mapping epochs (corresponding to two cardinal sweep directions) were always followed by two blank epochs. The load task was ongoing during the first of these blanks, while the second blank was a rest period during which participants were required to fixate a dot at the centre of the display (serving as a common baseline for both load conditions). After three mapping runs, participants completed two HRF runs with 5 photic bursts per load condition. After the first 5 photic bursts participants carried on solving the load task for 12 blank TRs (or 30.6 s), followed by a rest period of 24 TRs (60.12 s). Then the task resumed (with the other load condition) for another 5 photic bursts and 12 blank TRs.

To assess fixation compliance we used an EyeLink 1000 MRI compatible eyetracker (http://www.sr-research.com/), tracking gaze position of the left eye. Due to technical problems and a restricted field of view for the eyetracker we could only collect eye data for 16 participants.

Image Acquisition and Pre-processing

All functional and structural scans were obtained with a Tim Trio 3T scanner (Siemens Medical Systems, Erlangen, Germany), using a 32-channel head coil. However, the front part of the head coil was removed for functional scans, leaving 20 effective channels (this way restrictions of participants' field of view were minimised). Functional images for the main experiment were acquired with a gradient echo planar imaging (EPI) sequence (2.3 mm isotropic resolution, matrix size 96 x 96, 30 transverse slices per volume, acquired in interleaved order and centred on the occipital cortex; slice acquisition time 85 ms, TE 37 ms, TR 2.55 s). We obtained 148 volumes per mapping run and 124 volumes per HRF run (196 and 172 volumes, respectively, for mapping and HRF runs including both load conditions; including four dummy volumes at the beginning of each run). In between mapping and HRF runs we acquired B0 field maps to correct for geometric distortions in the functional images caused by heterogeneities in the B0 magnetic field (double-echo FLASH sequence with a short TE of 10 ms and a long TE of 12.46 ms, 3x3x2 mm, 1 mm gap). Finally, we acquired two T1-weighted structural images of each participant. The first structural image was obtained with the front part of the head coil removed, using an

MPRAGE sequence (1 mm isotropic resolution, 176 sagittal slices, matrix size 256 x 215, TE 2.97 ms, TR 1900 ms). For the second structural image we used the full 32-channel head coil with a 3D MDEFT sequence ([S4]; 1 mm isotropic resolution, 176 sagittal partitions, matrix size 256 x 240, TE 2.48 ms, TR 7.92 ms, TI 910 ms).

All image files were converted to NIfTI format and pre-processed using SPM 8 (http://www.fil.ion.ucl.ac.uk/spm/software/spm8/). The first four volumes for each run were discarded to allow for the T1 signal to reach steady state. The remaining functional images were mean bias corrected, realigned, unwarped (using voxel displacement maps generated from the fieldmaps [S5]), co-registered (with the respective anatomical MDEFT scan for each participant, using the MPRAGE scan as an intermediate step) and smoothed with a 4 mm Gaussian kernel. The anatomical MDEFT scan was used to reconstruct the cortical surface with FreeSurfer (http://surfer.nmr.mgh.harvard.edu) and the functional time series were projected onto the surface, detrended and z-normalised for each run and vertex. Finally, runs containing both load conditions were split, so that all data could be separated according to condition.

Data Analysis

Data analysis was conducted using FreeSurfer (http://surfer.nmr.mgh.harvard.edu) and MATLAB (Mathworks, Ltd.), including SPM 8 (http://www.fil.ion.ucl.ac.uk/spm/software/spm8/) and a custom MATLAB toolbox for population receptive field analysis and transforming data between volume and surface space. All data analyses were restricted to a mask of the posterior part of the brain, including occipital and inferior parietal cortex.

To estimate the individual, hemisphere and condition specific hemodynamic response function (HRF), we first identified visually responsive vertices within the mask (defined as vertices with an average positive response > 1 standard error for the first five volumes after each photic burst in an HRF run) and averaging the signal measured for all 10 photic bursts per scan run. We then fitted a double gamma function [S6] with four free parameters to the average stimulus evoked response of all visually responsive vertices. The fitted parameters corresponded to the latency of the HRF response and undershoot as well as their amplitudes (one parameter for the ratio of peak and undershoot amplitudes plus an absolute scale factor). To compare the amplitude of stimulus-evoked responses in the periphery between load conditions we compared condition and hemisphere specific HRF amplitudes for those runs containing both conditions and a common baseline (n=26 hemispheres). We used paired t-tests to compare fitted parameters as well as raw amplitudes between conditions (two-tailed .05 significance level; for raw data the peak was defined as the maximum response obtained in either condition).

Population receptive field (pRF) modelling was based on the assumption of symmetric two-dimensional Gaussian pRFs and data from the two load conditions were fit independently to compare the two resulting sets of model parameters. Model fitting was performed in a similar fashion as described by Dumoulin & Wandell [S7]. The three pRF parameters (x and y coordinates of centre position and the standard deviation, σ) were fitted in a two stage procedure for each vertex. Model predictions were always based on the stimulus time course (coding spatial positions as stimulated, or not, for a given point in time) and spatial sensitivity according to the assumed pRF parameters. To compare model predictions with empirical BOLD time courses, predictions were convolved with the hemisphere and condition specific HRF estimates (see above). A first coarse fit consisted of an exhaustive grid search for the set of parameters providing the highest correlation between empirical and predicted time courses (grid size 15x15x34 for centre positions and σ, respectively). The obtained parameters then formed the initial values for a subsequent fine fit, aiming to minimise model prediction error using a simplex method [S8, S9]. This step also included a scaling factor, β,. The resulting parameter maps were smoothed with a surface based kernel of 5 mm FWHM.

We delineated retinotopic regions of interest (V1-3, V3A/B, and IPS0/1) based on data from the low load condition (but area boundaries were checked and found to be consistent between conditions). Centre position coordinates of vertices were transformed into polar angle and eccentricity, colour coded and projected as maps on the inflated cortical surface. Boundaries of V1-3 were drawn according to standard procedures [S10] at meridian mirror reversals of polar angle. Dorsal areas IPS0/1 could only be delineated for a subset of 24 hemispheres and data within dorsal areas was patchy for most hemispheres. Definitions of dorsal retinotopic areas followed Wandell *et al.* [S11]: IPS0/1 was defined as the area extending along the intraparietal sulcus from the dorsal boundary of V3A/B to the next representation of the upper vertical meridian (with V3A/B being defined as the area anterior and superior of V3, bordering on a representation of the upper vertical meridian dorsally).

We compared pRF eccentricity and size (σ) between conditions. Eccentricity was defined as the distance between fixation and the estimated pRF centre position. Vertices with a model fit of $R^2<.05$ in either of the conditions were not taken into account for statistical comparisons (note that we fitted the model to the complete times-series; comparable analyses fitting averaged time-series have fewer degrees of freedom and thus yield nominally higher R^2 values). We calculated differences on a vertex-by-vertex basis (i.e. parameters for a given vertex were compared between conditions) and as relative change compared to the size of the pRF under low load (absolute differences divided by σ). All analyses were restricted to eccentricities between one and seven degrees thus avoiding inner- and outermost pRFs, which were only partially mapped. The resulting differences (and absolute values) were averaged for each region of interest and hemisphere. We then applied an outlier criterion to the data of each region of interest independently, removing data points further than 3.5 robustly estimated standard deviations from the mean (standard deviations estimated based on median absolute deviation [S12]). Note that the effects we reported did not hinge on outlier removal and persisted when potential outliers were left in the analysis (Supplemental Results and S1, G-I). Differences were tested against zero based at the group level with one sample t-tests (two-tailed .05 family-wise error significance level). Significance levels were corrected for testing multiple regions of interest (V1-3 and IPS) following the Holm-Bonferroni method [S13]. For plotting we binned results in eccentricity bands of half a degree visual angle, based on pRF center positions according to low load data. The outlier exclusion criterion described above was applied to data from each bin independently for plots.

Note that the forward modelling approach we used to estimate pRFs explicitly incorporated the hemodynamic response function (HRF). Perceptual load could have an effect on the HRF that is unrelated to the spatial preference of the underlying neural populations (e.g. due to changes in neural amplitude [S14], response latency and/or HRF shape). We aimed to control for potential HRF confounds by collecting additional data for each participant and estimating the visual cortex HRF on a hemisphere and condition specific basis (see above). For our main pRF analyses we used these condition and participant-specific HRFs. This also allowed us to explicitly test for effects of condition on BOLD amplitude by comparing HRF estimates between conditions (Figure S1 B). To further test the effects of condition-specific hemodynamic response amplitude and profile, we repeated the main analyses swapping the condition-specific HRFs for each participant (Figure S1 D-F). Some control analyses involved fitting of a repeated measures general linear model (GLM, see below). For these analyses SPSS 21 (IBM, Armonk, New York) was used and degrees of freedom were Greenhouse-Geisser corrected if Mauchly's Test indicated violations of sphericity. For GLM analyses data points further than 3.5 robustly estimated standard deviations from the mean were replaced by the group mean (see above).

We compared eye movement data between conditions by calculating the average standard deviation (*S.D.*) of eye position across epochs in the mapping experiment (independently for horizontal and vertical axes and separately for each condition; Figure S1 C, left hand side). Note that simulations indicate pRF estimates can be biased by eye movements, but only if they are of considerable magnitude (c.f. Figure 6 in [S15]). To further test whether participants were biased in their eye movements towards following the mapping stimulus, the same analysis was repeated for epochs with horizontal and vertical bar sweeps separately. This allowed us to calculate an index of bias in eye position towards the stimulus as

$$\text{Bias} = (S.D._{\text{vertical}} - S.D._{\text{horizontal}} \mid \text{vertical stimulus sweep}) - (S.D._{\text{vertical}} - S.D._{\text{horizontal}} \mid \text{horizontal stimulus sweep})$$

(Figure S1 C, right hand side).

Supplemental Results

Behavioural and Eye Data

Participants were significantly less sensitive (t_{25}=11.83, $P<10^{-11}$) and slower (t_{25}=15.75, $P<10^{-13}$) when detecting high vs. low load targets, indicating successful manipulation of perceptual load (Figure S1 A).

Analysis of eye data obtained in the scanner (n=16) indicated a high degree of gaze stability (average SD < 1 degree visual angle for both conditions and axes; Figure S1 C, left hand side). Participants' gaze was slightly more stable in the high load condition (vertical axis: t_{15}=3.14, P<0.01; horizontal axis: t_{15}=1.69, P=0.11, *n.s.*). Note that this is the opposite direction of what would explain the observed effects on pRF size estimates in V1-3.

To test whether participants were biased to move their eyes towards the mapping stimuli we calculated an index of eye movement bias towards the axis along which the stimulus travelled (see above, Supplemental Experimental Procedures). Participants were not biased to follow the mapping stimulus with their gaze in either condition (low load: t_{15}=-0.56, P=0.59, *n.s.*; high load: : t_{15}=0.13, P=0.90, *n.s.*; Figure S1 C, right hand side).

Hemodynamic Response Profiles

For each participant we acquired additional data to estimate the individual hemodynamic response profile for each condition (see above, Supplemental Experimental Procedures). In order to control for possible amplitude effects and other HRF differences between conditions we used these individual (hemisphere) and condition-specific HRFs in our forward model. This also allowed us to compare the hemodynamic responses to photic bursts across conditions for HRF runs containing both conditions (sample B; see above). The peak amplitude of raw measurements to estimate the HRF was higher under low compared to high perceptual load (t_{25}=3.04, *P*<.01; Figure S1 B). A similar, but non-significant trend was observed for the amplitudes of the fitted HRFs (t_{25}=1.91, *P*=.07). No significant difference was observed for any of the other fitted parameters (response latency: t_{25}=0.02, *P*=.99 undershoot latency: t_{25}=0.98, *P*=.34; peak/undershoot ratio: t_{25}=0.75, *P*=.46).

To test the effects of HRF profiles on pRF estimates we re-analysed data from V1-V3 using condition-swapped HRFs. Swapping HRFs between conditions had an effect on estimated pRF sizes, with pRFs up to ~3° eccentricity being smaller under high perceptual load, however this effect was not significant (Figure S1 D,E). Most importantly, our main results were robust with regard to swapping HRFs: Under high perceptual load pRFs from about 3° eccentricity were still significantly bigger (in V2 and V3, non-significant trend for V1; Figure S1, D,E) and more eccentric (Figure S1 F).

Radial Gradient of Response Amplitudes as a Potential Confound?

Note that previous studies focussing on the effect of central load on BOLD amplitude for peripheral stimulation found the effect of load to decline from about eight degrees eccentricity (e.g. [S14], Figure 8B). This kind of eccentricity dependence of amplitude effects is unlikely to affect our data given we only stimulated the innermost nine degrees of the visual field and included data from pRFs with centre position up to seven degrees eccentricity. Nevertheless an interaction between perceptual load and eccentricity with regard to BOLD amplitude could introduce spurious pRF changes. Specifically, if high perceptual load has a suppressive effect on signal amplitudes that declines with eccentricity, this might yield a radial skew of pRFs under high load because neurons with more centrally located small receptive fields are down-weighted and the population signal is dominated by larger peripheral receptive fields. We conducted three further control analyses to rule out this potential confound for our main results.

First, we tested whether there was a condition by eccentricity interaction with regard to HRF amplitude. For this we binned the data used for comparison of HRF profiles (see above) by region of interest (V1-3) and eccentricity bands (1-7 degrees in steps of half a degree). Vertices were binned according to pRF fits for low load data. This allowed us to extract the HRF profile and fit a double gamma function for each region of interest and eccentricity bin in turn. Figure S2 A) shows the amplitudes of fitted HRFs by condition and eccentricity for V1-3 and Figure S2 D) shows the corresponding differences between conditions. To test for a condition by eccentricity interaction we fitted a separate repeated measures general linear model (GLM) to the data from each region of interest, with eccentricity and condition as within-subjects factors. The amplitude parameter of fitted HRFs did not systematically vary with eccentricity (V1: $F_{(2.05, 51.32)}=0.98$, $P=.38$; V2: $F_{(3.75, 93.82)}=2.37$, $P=.06$; V3: $F_{(3.80, 95.03)}=0.77$, $P=.67$). In line with our results for pooled vertices there was a trend for a main effect of condition in the direction of reduced amplitude under high perceptual load (that was statistically significant in V2; V1: $F_{(1, 25)}=1.82$, $P=.19$; V2: $F_{(1, 25)}=4.35$, $P<.05$; V3: $F_{(1, 25)}=4.06$, $P=.06$). Crucially, there was no interaction effect between condition and eccentricity with regard to HRF amplitude (V1: $F_{(2.51, 62.75)}=0.27$, $P=.99$, V2: $F_{(4.98, 124.61)}=1.36$, $P=.25$; V3: $F_{(3.96, 98.88)}=0.63$, $P=.64$).

A second control analysis compared the goodness of pRF model fits across eccentricity bands and conditions. If high attentional load induced a radial skew of pRFs this should lead to a reduced goodness of fit of our symmetric model for the high perceptual load condition. Figure S2 B) shows the coefficient of determination by eccentricity and condition for each region of interest. Figure S2 E) shows the corresponding differences between conditions. Again, we used repeated measures GLMs to test for a main effect of condition on goodness of fit and potential interactions with eccentricity. Overall goodness of fit varied with eccentricity (V1: $F_{(3.31, 175.74)}=36.45$, $P<.001$; V2: $F_{(4.82, 255.79)}=17.44$, $P<.001$; V3: $F_{(3.35, 177.34)}=36.04$, $P<.001$). Reassuringly goodness of fit in either condition was highest for a similar eccentricity range as the one for which we observed the clearest evidence for pRF size and eccentricity effects (c.f. Figure S2 B) and Figure 1 C) and D)). There also was a trend for goodness of fit to vary with condition (that was statistically significant in V1 ; V1: $F_{(1, 53)}=8.60$, $P<.01$; V2: $F_{(1, 53)}=3.43$, $P=.07$; V3: $F_{(1, 53)}=2.84$, $P=.10$). Crucially, this effect was in the opposite direction of what a systematic skew of pRFs in the high load condition would predict – high perceptual load went along with *better* fits. Finally, there was no significant interaction between condition and eccentricity with regard to goodness of fit (V1: $F_{(2.55, 134.97)}=1.01$, $P=.38$, V2: $F_{(4.60, 244.02)}=1.88$, $P=.10$; V3: $F_{(3.11, 164.56)}=1.38$, $P=.25$).

A third control analysis tested the hypothesis that high attentional load induces radial skew in the spatial response profile of vertices. For this we re-analysed the pRF data using a model-free reverse correlation approach (c.f. [S16] for a similar approach). In short, the stimulus display was down-sampled to a 100x100 pixel matrix and the stimulus time-course for each pixel convolved with the condition specific HRF. The empirical time-course of each vertex was then correlated with and multiplied by these pixel-specific predictions yielding two types of reverse correlation profiles per vertex. The first profiles comprised *correlation coefficients* between pixel-stimulation and vertex-activation. The second profile was an activation profile indicating the vertex' responsiveness for each pixel. The activation map was thresholded by the correlation profile to exclude any activations that were not significantly ($P<0.01$, Bonferroni corrected by the number of pixels) correlated with the vertex' time-course. This step was used in order to minimize the influence of artifacts that arise due to correlations between pixels in the input stimulus (e.g. using a vertical bar stimulus pixels along the bar would always be stimulated simultaneously). These thresholded activation profiles were then used for all further analyses.

The resulting response profiles were sorted by eccentricity and polar angle according to the pRF centre positions of the respective vertices according to the main analysis. Specifically, eccentricity bins spanned from one to seven degrees visual angle in steps oh half a degree. Each eccentricity bin was then further subdivided in eight polar angle bins corresponding to steps 45 degrees from the right horizontal meridian. pRF profiles in each of these eccentricity-by-polar angle bins were peak centred and averaged for data from each condition and participant individually. Within each eccentricity band the average profiles corresponding to different polar angle subdivisions were then rotated to a common reference frame such that the horizontal left-right axis corresponded to the central-radial axis going through the middle of the polar angle bin in the original frame. This allowed us to average response profiles across polar angle bins but at the same time preserve sensitivity to hypothetical radial skew. Finally, the resulting averages for each eccentricity bin were normalised to a scale from zero to one.

To quantify skew along the radial axis for each eccentricity band we calculated the ratio of the volume under the curve to the right of the vertical axis (i.e. the radial hemi-field) vs. the volume on the left (central) hemi-field. Ratios greater than one indicated radial bias while ratios less than one pointed to central bias. Figure S2 C) shows the resulting ratios by eccentricity and condition and for each region of interest. Figure S2 F) shows the corresponding differences between conditions. Response profiles overall showed a small central bias that was not statistically significant (averaged across eccentricity bins ratios were between 0.95 and 0.99 for high load and between 0.96 and 0.99 for low load; all $t \leq 1.90$, all $P \geq .07$). Crucially, there was no difference regarding bias across conditions (V1: $F_{(1, 27)}=0.10$, $P=.76$; V2: $F_{(1,27)}=0.07$, $P=.80$; V3: $F_{(1, 27)}=0.03$, $P=.87$) and there was also no significant difference between eccentricity bands (V1: $F_{(4.12, 111.15)}=1.01$, $P=.41$; V2: $F_{(3.60, 97.10)}=1.11$, $P=.35$; V3: $F_{(5.46, 147.31)}=2.18$, $P=.05$). Figure S2 G-I shows group level averages of reverse correlation response profiles by eccentricity for each region of interest. Horizontal cross sections of the response profiles illustrate their general Gaussian nature. Furthermore, average reverse correlation profiles on the single subject and eccentricity band level were well matched by the isotropic Gaussian model we used (R^2 in either condition and V1-3 ~.7; data not shown). This was true despite apparent bar artefacts introduced by the stimuli we used (c.f. the ‘wheel spoke’ pattern in Figure S2 G-I). However, we cannot rule out that model-fit varies as an interaction between model and stimulus type which could limit the generalizability of our findings.

Taken together we tested three predictions stemming from the hypothesis that a radial gradient in load-induced amplitude effects would confound our main results. None of these predictions was met. Specifically, we found no evidence for an eccentricity dependent effect of perceptual load on response amplitudes, replicating the findings by Schwartz *et al.* [S1] who only found such an effect for visual field locations more peripheral then the ones we investigated. Furthermore, we found no evidence for reduced goodness of fit of pRF model under high perceptual load – to the contrary, model fits were slightly *better* for the high perceptual load condition. Finally, reverse correlation of pRF response profiles showed no evidence of a load-induced deviation from symmetry. We conclude that it is extremely unlikely that the load-induced effects on pRF size and eccentricity are confounded by eccentricity dependent amplitude effects.

Outlier Exclusion

Our analysis included an automatic removal of potential outliers (see above, Supplemental Experimental Procedures). To test for the effect of these potential outliers we repeated the analysis including all datapoints. Including potential outliers in the analyses left the overall pattern of absolute changes in pRF size qualitatively unchanged (Figure S1 G). However, it enhanced the overall pRF size changes we observed (V1: mean=23.24% +/- s.e.m.=6.29%, t_{53}=3.69, P_{FWE} <0.01; V2: mean=19.17% +/- s.e.m.=5.49%, t_{53}=3.49, P_{FWE} <0.01; V3: mean=15.07% +/- s.e.m.=4.77%, t_{53}=3.16, P_{FWE} <0.01). Potential outliers markedly skewed the results towards a greater increase of relative pRF sizes under high perceptual load for the innermost eccentricity bands (Figure S1 H). Note that given the small absolute sizes of these pRFs the relative measure is more prone to yield extreme outliers.

The pattern of eccentricity changes in V3 (mean=11.12% +/- s.e.m.=3.00%, t_{53}=3.14, P_{FWE}<0.05) remained qualitatively unchanged while the eccentricity changes in V1 (mean=4.81% +/- s.e.m.=6.06%, t_{53}=0.79, P_{FWE} =0.86) and V2 (mean=6.46% +/- s.e.m.=3.20%, t_{53}=2.02, P_{FWE} =0.15) were reduced and became statistically insignificant when potential outliers were included in the analysis (Figure S1 I).

Preliminary Results for IPS0/1

Data from IPS did not indicate a significant change of pRF size for this area (mean=-3.44% +/- s.e.m.=4.57%, t_{18}=-0.75, P_{FWE} =1; Figure S1 J,K).

The eccentricity effect on pRFs observed in earlier areas was reversed in IPS (Figure S1 L). pRF eccentricity *de*creased under high perceptual load (mean=-14.03% +/- s.e.m.=4.35%, t_{16}=-3.23, P_{FWE} <0.05). This effect was strongest from about 4.5° eccentricity.

Supplemental References

S1. Schwartz, S., Vuilleumier, P., Hutton, C., Maravita, A., Dolan, R. J., and Driver, J. (2005). Attentional load and sensory competition in human vision: modulation of fMRI responses by load at fixation during task-irrelevant stimulation in the peripheral visual field. Cereb. Cortex *15*, 770–86.

S2. Brainard, D. H. (1997). The Psychophysics Toolbox. Spat. Vis. *10*, 433–6.

S3. Pelli, D. G. (1997). The VideoToolbox software for visual psychophysics: transforming numbers into movies. Spat. Vis. *10*, 437–42.

S4. Deichmann, R., Schwarzbauer, C., and Turner, R. (2004). Optimisation of the 3D MDEFT sequence for anatomical brain imaging: technical implications at 1.5 and 3 T. Neuroimage *21*, 757–67.

S5. Hutton, C., Bork, A., Josephs, O., Deichmann, R., Ashburner, J., and Turner, R. (2002). Image distortion correction in fMRI: A quantitative evaluation. Neuroimage *16*, 217–40.

S6. Friston, K. J., Fletcher, P., Josephs, O., Holmes, A., Rugg, M. D., and Turner, R. (1998). Event-related fMRI: characterizing differential responses. Neuroimage *7*, 30–40.

S7. Dumoulin, S. O., and Wandell, B. A. (2008). Population receptive field estimates in human visual cortex. Neuroimage *39*, 647–60.

S8. Nelder, J. A., and Mead, R. (1965). A Simplex Method for Function Minimization. Comput. J. *7*, 308–313.

S9. Lagarias, J. C., Reeds, J. A., Wright, M. H., and Wright, P. E. (1998). Convergence Properties of the Nelder--Mead Simplex Method in Low Dimensions. SIAM J. Optim. *9*, 112–147.

S10. Sereno, M. I., Dale, A. M., Reppas, J. B., Kwong, K. K., Belliveau, J. W., Brady, T. J., Rosen, B. R., and Tootell, R. B. (1995). Borders of multiple visual areas in humans revealed by functional magnetic resonance imaging. Science *268*, 889–93.

S11. Wandell, B. a, Dumoulin, S. O., and Brewer, A. a (2007). Visual field maps in human cortex. Neuron *56*, 366–83.

S12. Hampel, F. R. (1974). The Influence Curve and its Role in Robust Estimation. J. Am. Stat. Assoc. *69*, 383–393.

S13. Holm, S. (1979). A simple sequentially rejective multiple test procedure. Scand. J. Stat.

S14. Schwartz, S., Vuilleumier, P., Hutton, C., Maravita, A., Dolan, R. J., and Driver, J. (2005). Attentional load and sensory competition in human vision: modulation of fMRI responses by load at fixation during task-irrelevant stimulation in the peripheral visual field. Cereb. Cortex *15*, 770–86.

S15. Levin, N., Dumoulin, S. O., Winawer, J., Dougherty, R. F., and Wandell, B. A. (2010). Cortical maps and white matter tracts following long period of visual deprivation and retinal image restoration. Neuron *65*, 21–31.

S16. Lee, S., Papanikolaou, A., Logothetis, N. K., Smirnakis, S. M., and Keliris, G. A. (2013). A new method for estimating population receptive field topography in visual cortex. Neuroimage *81*, 144–57.